Mechanical Properties, Metallurgical Characteristics and Anisotropy of Additive Manufacturing of 316L

D. Moreno* ⬤, Y. Nahmana, O. Nafman, O. Kam, B. Wolfman, A. Y. Cohen, M. Shapira

Bet Shemesh Engines LTD, FAA & EASA, Bet Shemesh, Israel
Email: *danielm@bsel.co.il, yohanan@bsel.co.il, orel@bsel.co.il, ork@bsel.co.il, borisw@bsel.co.il, arielc@bsel.co.il, shapira@bsel.co.il

Abstract

Additive manufacturing (AM), while enabling the production of parts with complex geometries, presents new challenges. In particular, the achievement of the basic mechanical properties of the alloy must be ensured. In general, the strength-ductility properties of metals depend strongly on their microstructure, and controlling these properties requires paying attention to the alloy composition, processing technique and heat treatments. Austenite 316L stainless steel parts produced by AM demonstrate good ductility and high yield strength—higher than that obtained with annealed 316L. Some preferred orientation of the mechanical properties was found as a function of the laser path, namely, the Young's modulus varied with respect to the angle between the build direction and the normal to the build direction. In the present study, samples of AM 316L in three orientations relative to the print direction (0˚, 45˚ and 90˚) are compared to a forged sample. Mechanical properties, scanning electron microscopy-SEM fractography, energy dispersive X-ray spectroscope-EDS analysis of the fracture and optical cross section images of the samples along the stress tension after the failure are presented.

Keywords

SS316L, Additive Manufacturing (AM), Preferred Orientation, Mechanical Properties, Young's Modulus

1. Introduction

The well-known austenitic 316L stainless steel alloy, which combines outstanding corrosion resistance, ductility, moderate to high-temperature performance, high vacuum properties, and suitability for structural applications, is one of the

most attractive industrial alloys for a large variety of environments. However, it displays low strength and wear resistance, which limits its high-performance applicability, and it is also difficult to make complex-geometry parts with it. Additive manufacturing (AM), carried out layer-by-layer with a deposition technique, offers new opportunities for producing complex-geometry parts, but also presents new challenges with regard to achieving basic required mechanical properties [1] [2]. The AM process has many aspects that need to be considered, including thermal phase transformation during a transient process in accordance with the thermodynamic roles of the metal components. During the last few years, research on the metallurgical properties of additive manufactured (3D printed) parts have been reported for a wide range of stainless steels [3] and AM is an ongoing research topic.

In general, the strength-ductility properties of metals depend strongly on their microstructure, which, in turn, depends on their compositional engineering processing technique and heat treatment for alloy improvement. Specifically, austenite 316L stainless steel made by AM has been found to display good ductility and high yield strength, in fact higher than that obtained for annealed 316L; this may be attributed to the high dislocation density and small microstructure grains [4].

There are several methods currently employed for AM. One of the prototyping technologies in layer-by-layer AM is Selective Laser Sintering (SLS). Laser welding has a much higher energy density in comparison to arc welding methods; the laser achieves high melt pool penetration and low base metal effects in the heat effected zone (HAZ) [5] [6]. In addition, the selected laser melting (SLM) process could offer the advantage of facilitating reinforcement of the metal by adding composite additives such as TiB_2 and TiC compounds with a powder-bed-based AM process, and by either direct mixing or ball milling powder use [3]. The structured development of processing conditions for single lines, single layers and multiple layers of material was reported in [7] [8]. The process involved many physical aspects, such as optical absorption and reflection, heat and mass transfer, phase transformation, solidification front formation, surface tension and chemical reactions [9]. The bonding mechanism of different powder particles was described from the metallurgical point of view in [10]. The mechanism is based on the use of a local mobile Gaussian heat source embodied in a scanning laser beam to re-solidify the metal powder melt beds, followed by sintering to nearly full density and reconstruction of the manufactured designed part. The combination of the re-solidification done sequentially layer-by-layer, the metal conductivity and the heat transfer lead the solidified bulk to adopt the preferred orientation of the new solidified grains. During AM, the Gaussian source beam heating and the powder bed interaction are very brief and depend on the scanning speed of the beam; as a result, rapid solidification is obtained. A structure of dendrites and fine-grains is obtained along the beam orientation or perpendicular to the applied layer. In addition, the 3D laser tech-

nique produces specific discontinuities, identified as micro-cracks, gas porosity and faceted voids [11]-[16]. In order to improve the density, SLS was needed for the manufacturing process in hard metals. In [8], some preferred orientation of the mechanical properties was found in correlation to the laser path. Most acceptable parts were manufactured with layer thicknesses around 50 - 80 μm and binder saturation of 60% - 70% [16]. Also, post processing based on the heat treatment sintering profile with suitable temperatures and time durations and proper atmospheres lead to good densification and improvement of the mechanical properties. However, in the case of SS316L, increasing the temperature to 1360°C - 1380°C during heat treatment of 4 - 6 h in a vacuum noticeably enhances some properties [17]. Improvement of the mechanical properties due to the AM technique is a curious issue and needs further investigation. Further, the directional effect of the AM process with regard to differences in the mechanical properties also needs further examination. Two decades after the first AM techniques were developed, typically anisotropic properties are still found. Experimental work and modelling of the anisotropic elastic properties, represented by the Young's modulus, were reported recently [18]. The lowest Young's modulus was observed along the build direction, rather than along the normal direction, which showed isotopic properties that correlate with the overall elastic behavior. The Young's modulus varied with respect to the angle with the build direction; this is attributed to the stiffness of the part, based on basic principles of elasticity in the matrix of the lattice structure [19] [20]. Moreover, the Young's modulus and the elastic physical specifications of FCC polycrystalline materials based on the Voigt-Reuss approximation showed good agreement with the experimental results, and could offer a good explanation for the change in the Young's modulus [21].

In the present study, 316L 3D printed samples with three orientations: 0°, 45° and 90°, are compared to forged and heat-treated samples. Mechanical properties, SEM fractography, EDS analysis of the fracture and optical cross section images of the sample along the stress tension after failure are presented.

2. Experimental Setup

A powerful 400-Watt Yb-fiber laser with high beam spot quality, good resolution and good precision was used in the present work. The SS316L spherical shaped powder with a generic particle size of 20 - 65 μm, and analyzed chemical composition shown in Table 1 was used. Samples were printed in three different directions: 0° (perpendicular to the printer beam), 90° (perpendicular to the feed layer/parallel to the printer beam) and 45° between the above two. The samples were machined to screw dog-bone mechanical property samples with the following dimensions: 1/2-13 UNC-2A screw, 6.5 mm diameter, 37 mm gauge length and a total length of 86 mm. The mechanical properties were measured in strain control mode at a 0.005 mm/min rate up to the yield stress value, and at a 1.00 mm/min rate to failure. In addition, forged SS316L samples after one hour of annealing at 1050°C were prepared for comparison. Screw grips were used for

Table 1. Powder chemical composition and EDS measurement (weight percent).

	Range	Fe	Cr	Ni	Mo	C	N	measurement
Powder Supplier documentation	Min.	Balance	17	13	2.35	-	-	bulk
	Max.	Balance	19	15	3.00	0.03	0.10	
EDS* Printed Samples	±3%	66.6	18.0	11.2	2.78	N.A.	N.A	surface
Forged sample Supplier documentation	N.A.	Balance	16.63	10.1	2.0	0.015	0.042	bulk

*High homogeneity was found in the printed samples.

the mechanical properties test. The tensile test was carried out with an Instron 5982 test machine at room temperature. After the mechanical tests were carried out, one side of each remaining sample was cut close to the neck to examine the cross section, and prepared for optical metallography inspection along the tensile axis to observe the flow deformation and the neck characteristics. The remaining sides of the samples were used for SEM/EDS (VEGAN-with integrated TESCAN Essence™ EDS) fractography investigation at high magnification to observe the fracture characteristics in the failure surface.

3. Results

Figure 1 shows the stress-strain plots of all the samples. Different behavior could be observed in the elastic and plastic characteristics for different load axis orientations of the sample; these could be correlated with and attributed to the feed layer build during manufacture. In the elastic range of the stress-strain plot, the highest value was obtained in the sample at 0˚ orientation; lower values were obtained at 90˚ and 45˚ with some similar linear behavior, and the lowest value was obtained in the forged annealed sample. The highest yield stress was obtained at 45˚ feeding orientation, while lower values were obtained for the 90˚ feeding orientation and the lowest for the forged and annealed sample. The highest UTS value was obtained at 0˚ and the lowest at 90˚. A comparison of the Young's modulus, UTS, yield and elongation values between the three different oriented samples and the 316L forged and annealed sample, tested similarly, is summarized in Table 2. The table includes the gauge dimeter D_0, gauge length before the tensile test L_{04D}, gauge length after the tensile test L_{f4D}, ambient temperature during the test and failure location for each sample. Figure 2 presents the optical metallography cross section near the neck for all the samples after the mechanical test. The optical metallography of the cross sections close to the center axis of each mechanical sample's rod close to the neck shows the flow failure zone. Four different neck fracture modes can be observed in the samples. Figure 2(a) shows a very small initially brittle zone at the perimeter of the sample, and then a ductile zone for the 0º feeding orientation sample; this behavior could be attributed to some micro-defects or micro-cracks on the surface of the sample.

Table 2. Mechanical property values obtained from the plots presented in Figure 1.

Specimen SS316L	Images	D_0 mm	L_{04D} mm	L_{f4D} mm	UTS (MPa)	Yield 0.2 (MPa)	Elongation (4D) %	Young's Modulus (GPa)	Ambient Temperature ˚C	Fracture Location
0˚	a	6.330	24.934	37.986	683	508	52.3	210	23.1	In Gauge Length
45˚	b	6.260	24.901	36.310	669	554	45.8	192	24.4	In Gauge Length
90˚	c	6.360	24.972	38.706	573	460	55.0	166	24.6	In Gauge Length
Forged	d	6.350	25.004	40.627	645	438	62.5	153	23.5	In Gauge Length
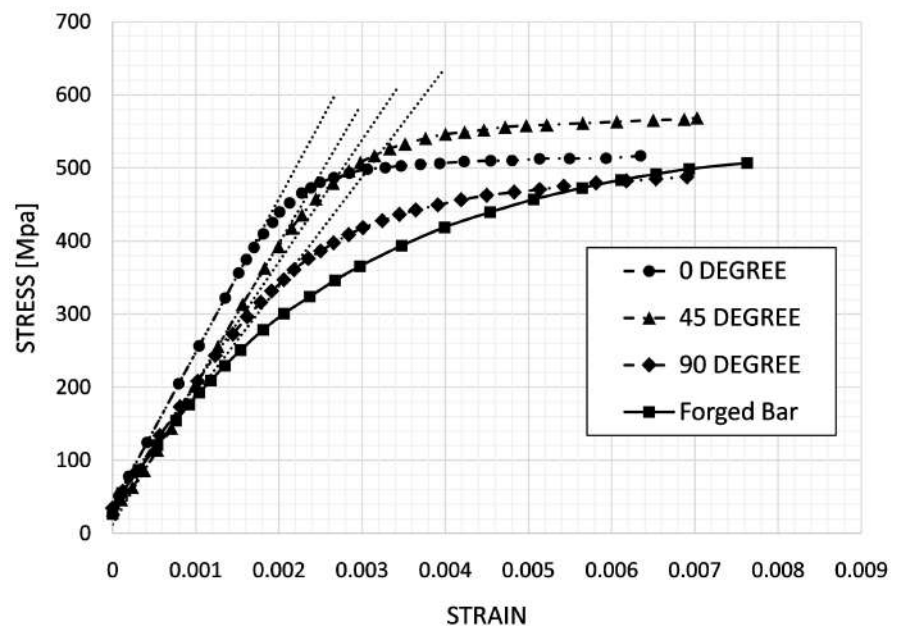
Figure 1. Stress-strain plot of the printed samples and the forged and annealed sample for comparison. Dashed lines show the linear behavior of the stress-strain curve to emphasize the modulus change obtained in the different samples.

In Figure 5(a) some brittle characteristics can be observed. The sample in Figure 2(b) shows almost ductile behavior for the 45˚ feeding orientation that could be attributed to the plane slips of the FCC lattice. It is very interesting to observe the 45˚ angle to the load stress axis of the failure surface. The sample in Figure 2(c) shows ductile flow in the neck and high deformation after the load overcame the yield stress (lowest yield in comparison to the other printed samples) at low stresses for the 90˚ case. Figure 2(d), presents the forged and annealed sample with preferred orientation structure that keeps the prior history of the sample during the forging process and shows very ductile behavior and the highest elongation.
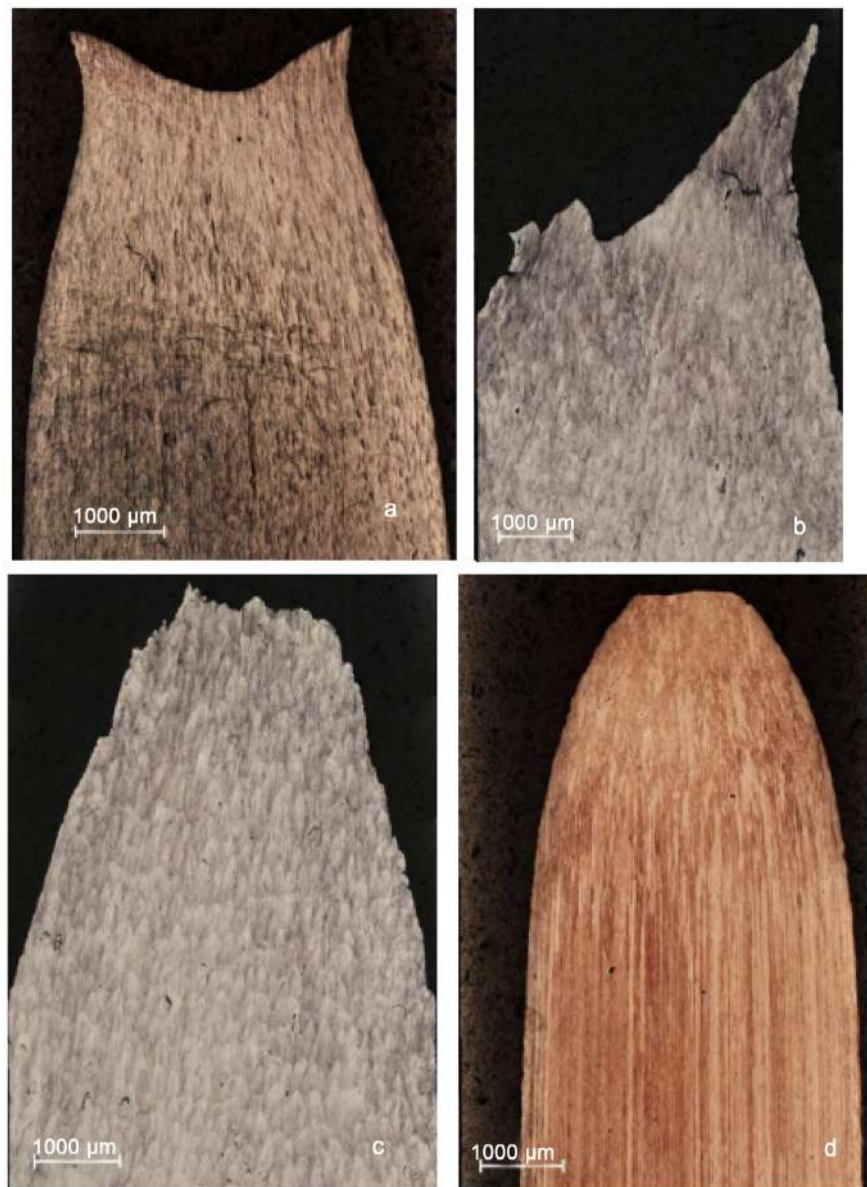
Figure 2. Optical metallography comparison of the necks obtained in the different samples. Initially brittle and then ductile at 0° (a), almost ductile at 45° (b), ductile flow neck at 90° (c) and very ductile obtained in the forged and annealed sample (d).

Figure 3 shows SEM images of the samples in the fracture area and at the perimeter of the sample close to the neck. Further information about the fractography of the samples can be obtained by enhancing the fracture area, as presented in Figure 4. All the samples presented dimples, but some differences can be observed. The size of the dimples in all the printed samples are sub-micron, in contrast to the forged sample, which is characterized by larger dimples with a typical size of tens of microns. In addition, the 0° oriented sample in Figure 4(a) shows a smooth topography of homogenous dimples in the failure area, in contrast to the observed 45° and 90° oriented samples in Figure 4(b) and Figure 4(c), where the tortuosity fractal dimensions of the fracture area are interrupted
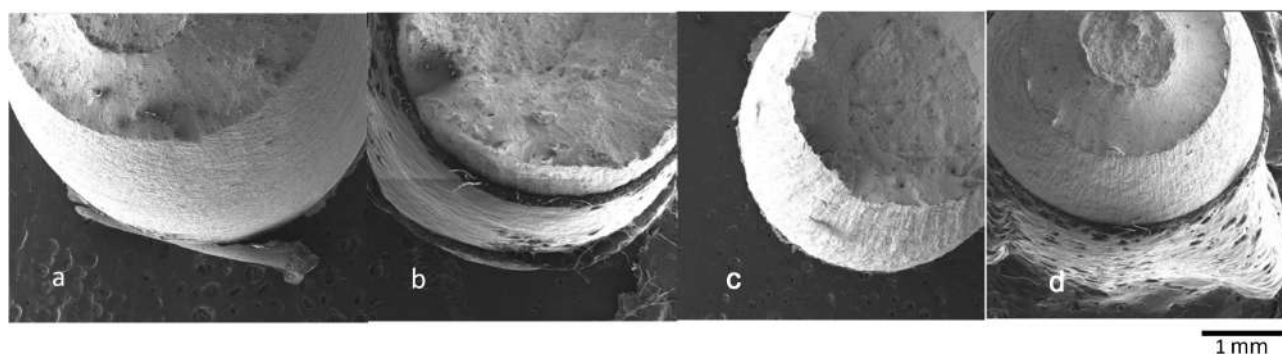
Figure 3. Comparison of SEM images of the fracture surface necks obtained in the different samples. The plastic deformation of the printed sample perpendicular to the feed beam at 0˚ (a), and 90˚ (c), and the forged and heat-treated sample (d) show similar behavior during failure. The 45˚ oriented sample shows deformation in two modes of normal stresses and shear stresses (b). The forged and heat-treated sample presented in **Figure 2(d)** appears for comparison.

by steps, ascents and descents—but the very same homogeneous dimples. In the 45˚ oriented sample, additional sharp discontinuities can be observed, as shown in **Figure 4(c)**. Larger dimples in the fracture area of the forged and heat-treated sample can be observed in **Figure 4(d)**.

Figure 4 also shows SEM images comparing the mechanical properties of the sample perimeter surfaces in the gauge length near the neck, and the flow mode of the slip deformation. The plastic deformation of the printed sample perpendicular to the feed beam during the print is shown for the 0˚ orientation in **Figure 5(a)**, 45˚ orientation in **Figure 5(b)** and 90˚ orientation in **Figure 5(c)**; these also show perimeter slip bands perpendicular to the stress. Preferred orientation grains (see **Figure 2(d)**) parallel to the stress orientation for the forged and heat-treated sample in **Figure 5(d)** show very small slip bands in the grains. As mentioned earlier, smooth fracture surfaces are evident in the 0º oriented sample and in the forged and heat-treated sample in **Figure 5(a)** and **Figure 5(d)**, respectively. The pronounced ascents and descents of the fracture surface in the 45˚ and 90˚ samples can be observed in **Figure 5(b)** and **Figure 5(c)**.

The parallel lines observed in the outside perimeter area of the gauge length of the samples represent the slip bands created during the deformation due to the axial stress. The same behavior can be observed in the forged sample, but the history of the preferred orientation grains shows limited slip in the grains and the creation of a rough surface of the deformed preferred oriented grains parallel to the axial stress applied. High magnification of the polished samples by SEM in **Figure 6** shows high void concentration for the 0˚ sample, voids and slip bands for the 45˚ and 90˚ samples, and slip bands and a very small amount of voids for the forged and heat treated sample.

4. Discussion

4.1. Thermodynamic Aspects

Generally, ductile and brittle failure can be attributed to the presence of a mixture
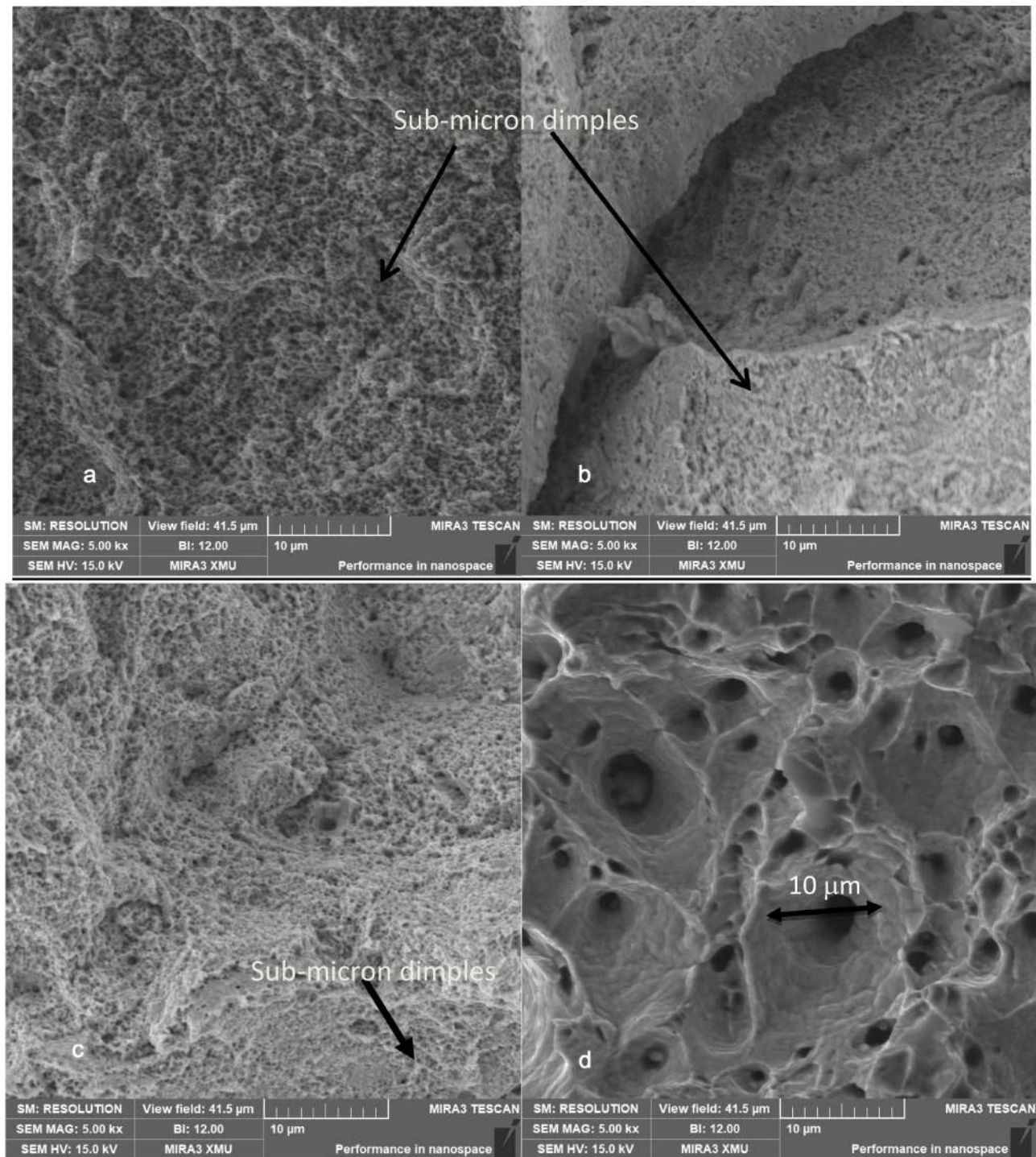
Figure 4. Comparison of SEM images of the fracture surfaces obtained in the different samples show characteristic ductile dimples of sub-micron size at 0° (a), 45° (b), and 90° (c) and very ductile behavior is obtained in the forged and annealed sample, with large dimples (d).

of cleavage deformation in the brittle metal cases, and micro-void formation and coalescence during ductile flow or shear slips at the macroscale [22] [23] [24]. Three different neck fracture modes that were observed in the manufactured samples can be attributed to the different macrostructures obtained during the
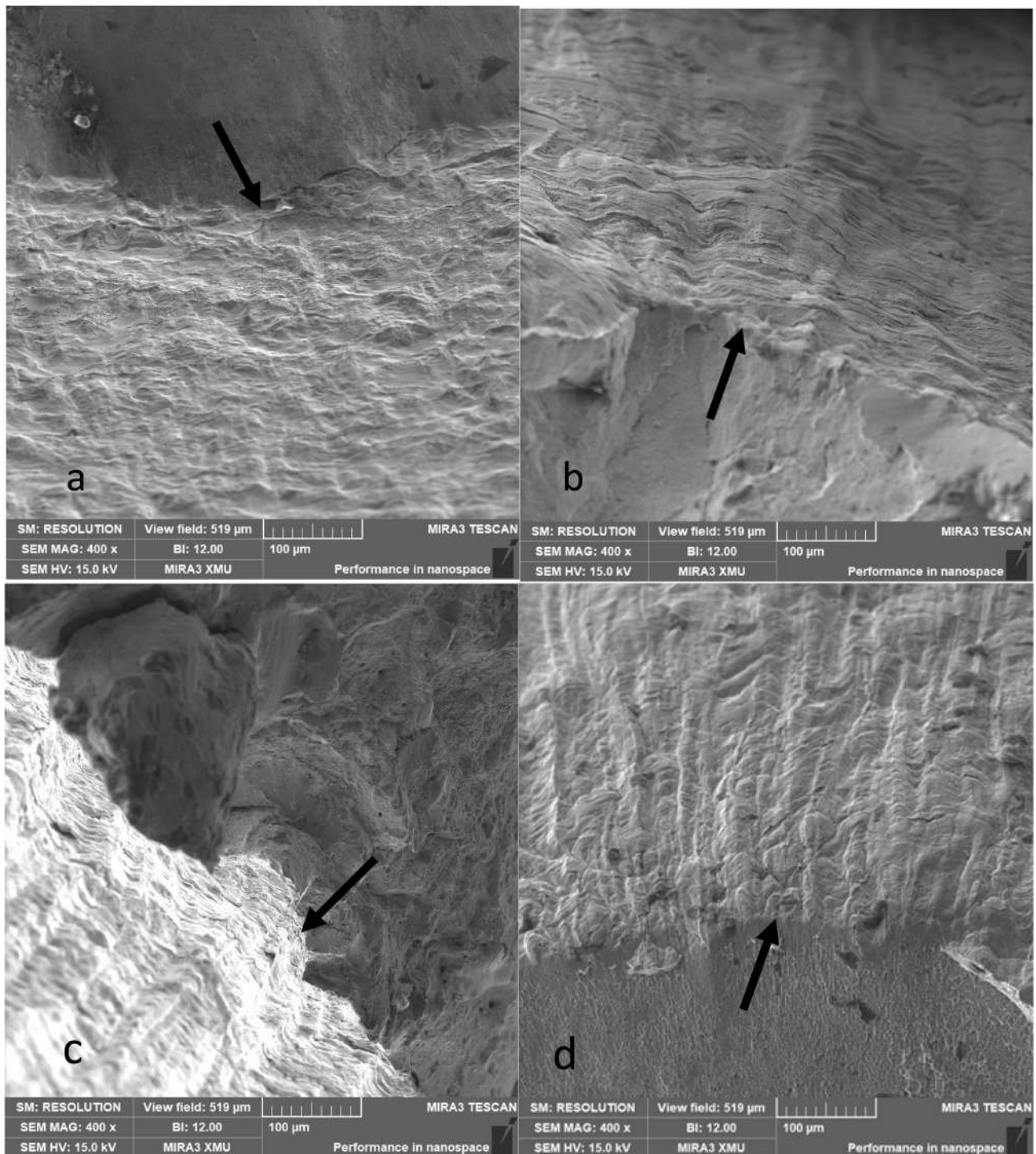
Figure 5. SEM image of the sample perimeter and the fracture surface in the same picture (arrows show the edge between the perimeter gauge length surface close to the neck and the fracture area). Images show slip bands at different directions and levels. The fracture surfaces present smooth fracture for the 0° sample (a), brittle surface for the 45° (b), and 90° (c) and very ductile and smooth surface for the forged and annealed sample (d).

different orientations of the feeding manufacturing in **Figures 2-6**. Thermal cycles are an inherent part of the successive layers printing process, where the uppermost layers in each additive spot undergo re-melting. This process is governed
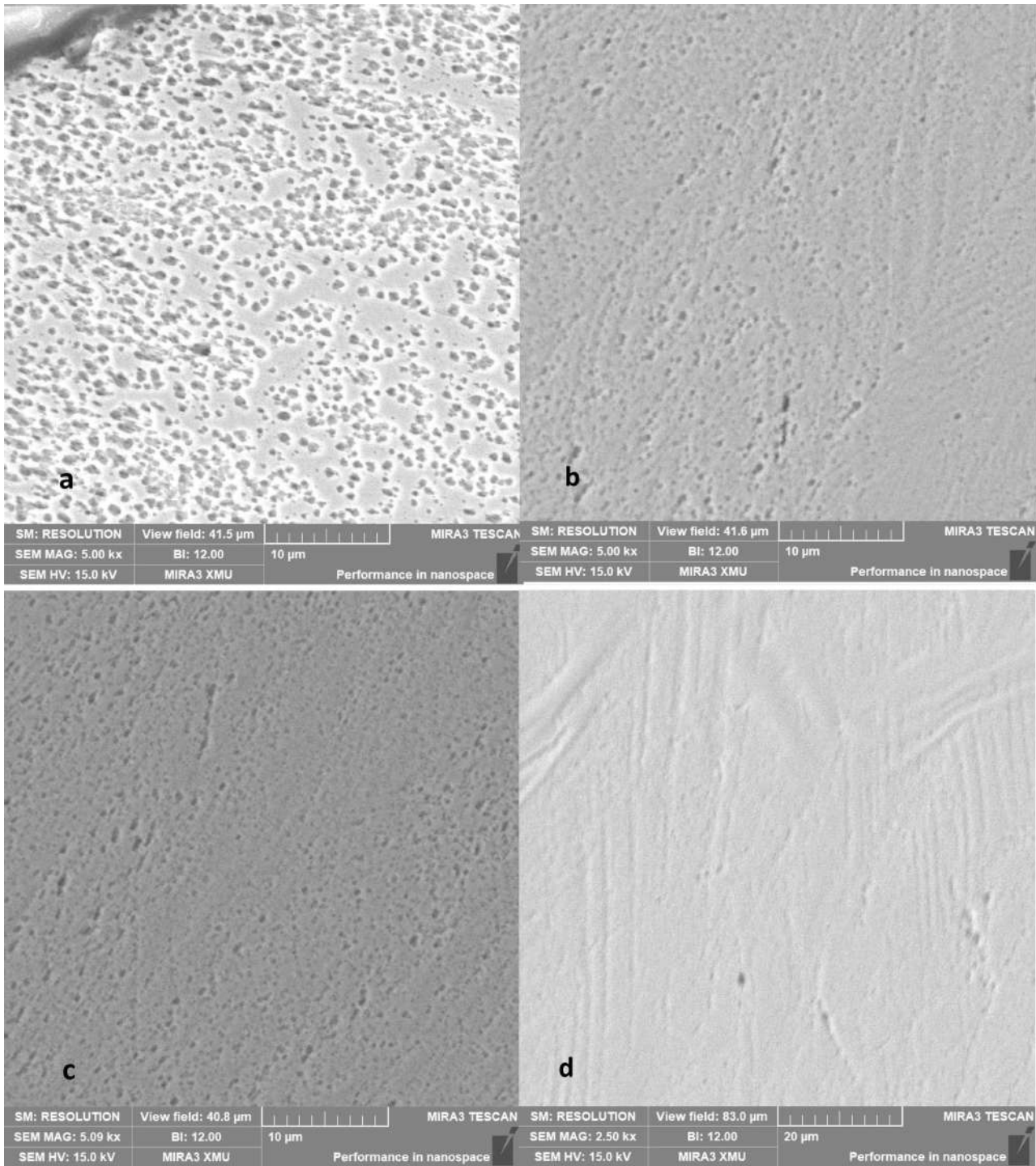
Figure 6. Comparison of SEM images of the magnified polished surfaces in **Figures 2(a)-(d)**, near the fracture, shows a combination of multi-voids, slips and twin deformations in printed samples at 45˚ (b), 90˚ (c) and the forged and annealed sample (d). Printed sample at 0˚ (a) shows multi-voids only after deformation close to the fracture.

by non-equilibrium solidification, and as result the microstructure is characterized by segregated cellular or dendritic structures and interfaces of Laves and carbides phases. However, the most important effect relevant to this study is the preferred orientation of the new grain solidification; the grains grow in the op-

posite direction to the heat transfer obtained by the temperature gradient between the micro-melt spot and the previously added already solidified zone. This thermodynamic solidification process yields the preferred properties attributed to the oriented solidification. Furthermore, some particles stay in the solid phase and do not melt; these are mainly carbides, and flow with the melted front and become impregnated in the dendrite or cellular orientation front.

4.2. Mechanical Aspects

Most metals are isotropic, so that their mechanical properties are the same in all directions. Furthermore, all solid materials exhibit reversible, nearly Hooke's Law-like, behavior for small enough strains or stresses in the proportional range, due to the bonding energy of the atoms. This behavior does not involve dislocation movements or slip planes, but only elastic properties. This Hooke's Law-like behavior gives the Young's modulus of the material and is the physical stiffness coefficient constant of the metal. It derives from the atomic interaction forces and may be changed by changing the temperature or pressure, but not by metallurgical interactions, although a preferred orientation of a microstructure in metals will lead to changes in the Young's modulus. It is well known that the value of elastic constants may change with the orientation of single crystal alloys and show anisotropy [25]. However, metals and ceramics can be treated with certain impurities, and metals can be mechanically worked to make their grain structures directional. The changes observed in the Young's modulus in the present study are attributed to the preferred orientation obtained due to the directional buildup of layers during AM. Basically, austenite SS316L has an FCC crystallographic structure at the grain level, and its isotropic behavior is attributed to the polycrystalline microstructure obtained in a conventional production technique. The anisotropy found in the AM samples, explained by the preferred orientation of the new grain growth, must be discussed. The anisotropy that is characteristic of AM-produced metal has been studied in a number of previous works [26] [27] [28].

4.3. Elastic Behavior

For instance, the mechanical behavior of an FCC nickel base single crystal was investigated during the last decades, and it was shown that the Young's modulus at <111> orientation achieves the maximum value (300 GPa), the minimum value is achieved at <001> orientation (125 GPa) and an intermediate value is achieved at <011> (230 GPa), at room temperature [26]. Also first-principles theory calculations were applied on crystalline silicon and on textured polycrystalline materials, and similar trend changes of the Young's modulus were observed [27] [28]. On the other hand, the mechanical properties measured in the same test show maximum yield at <111> (1320 MPa) and very similar values for the <001> and <011> directions (~875 MPa), at room temperature. In the same samples the highest UTS value was achieved at <111> (1700 MPa), a moderate

value at <001> (1300 MPa) and the lowest value at <011> (800 MPa). In the present study, the buildup layers direction, 90˚, corresponds to the new grain growth direction and is basically equivalent to the <001> direction, which is the fastest growth direction in FCC structures [29]. The AM technique produces very small grains, which we assume have some preferred orientation, but they are far from being mono-crystals. In our case, we assume that the 90˚ sample was solidified mostly parallel to the <001> direction, due to temperature gradient between the melting spot and the solidified bulk, and the preferred grow orientation in FCC metal [29]. According to this assumption, most of the grains in the 90˚ sample are supposed to be perpendicular to <001>. In other words, the 90˚ sample was solidified with polycrystalline grains with different directions between <010> and <100> and the lowest Young's modulus value (166 GPa). Theoretically, according to the crystal growth characteristics, the probability of obtaining grains with <111> directions in the 0˚ sample is negligible. With the same analogy, we can assume that the 45˚ sample has a higher probability of growing with some grains in the <111> direction. By applying this discussion to the results in this work, and from the theoretical point of view, the Young's modulus in the AM samples should have the lowest value at 90˚, as obtained in this study [26]. The samples manufactured at the 0˚ and 45˚ orientations do not have a specific orientation according to our analysis, but have higher Young's modulus values than the two other samples; this can be attributed to the orientation growth and the qualitative point of view.

4.4. Plastic Behavior

Plastic deformation involves many factors that must be taken in account, such as casting defects (that were not found in our inspections), interfaces and dislocation slips. As mentioned, the Smith's factor and dislocation slip directions could be relevant in the 90˚ sample's direction with some <001> orientation, but not in the other samples with the multi-directional orientations of their layers. The SEM images in **Figure 4(a)** show a smooth topography of homogenous sub-micron dimples in the failure area; this is in contrast to those observed in the 45˚ and 90˚ printed samples in **Figure 4(b)** and **Figure 4(c)**, where the flatness of the fracture area is interrupted by a non-flat surface with ascents and descents, but with the same homogeneous sub-micron dimples as shown in **Figure 4(a)**. Those complex surface topographies cannot explain the differences between the high yield stress in the 45˚ printed sample and the low yield stress in the 90˚ sample, but they emphasize the differences in the mechanical resistivity of the flow between the samples. Moreover, the cracks shown in the 45˚ printed sample in **Figure 4(b)** can explain the low deformation (45.8%) obtained due to possible pile-up of dislocations at the small grain boundary and a multidirectional structure rather than the higher deformation obtained in the 90˚ printed sample (55%). **Figure 5(a)** shows smooth deformation of the perimeter of the sample with a smaller difference in the total elongation (52.3%) in comparison

with the other samples, which can be attributed to the multi-voids shown in Figure 6(a), but less slip lines than observed in Figure 6(b) and Figure 6(d).

5. Conclusions

In this paper the mechanical properties, metallurgical characteristics and anisotropy of AM of 316L stainless steel were studied.

Anisotropy was found in the mechanical properties of AM printed samples of 316L stainless steel. This anisotropy is attributed to changes in the microstructure and to failed modes found in tested samples.

However, the mechanical properties of the AM printed samples in all directions, in terms of: Young's modulus, yield stress and UTS, show better values in comparison to the forged sample. On the other hand, the elongation of the forged and heat-treated sample is higher and thus it comprises a softer material in comparison to the AM printed samples.

The lowest value found for the Young's modulus at 90˚ is attributed to the preferred orientation growth in the AM samples due to the deposition of the layers, the thermal process and the solidification front. These results are consistent with the basic theory outlined in this study.

Conflicts of Interest

The authors declare no conflicts of interest regarding the publication of this paper.

References

[1] Thompson, M.K., Moroni, G., Vaneker, T., Fadel, G., Campbell, R.I., Gibson, I., Bernard, A., Schulz, J., Graf, P., Ahuja, B. and Martina, F. (2016) Design for Additive Manufacturing: Trends, Opportunities, Considerations, and Constraints. *CIRP Annals*, **65**, 737-760. https://doi.org/10.1016/j.cirp.2016.05.004

[2] Sun, C.H. and Shang, G.Q. (2021) On Application of Metal Additive Manufacturing. *World Journal of Engineering and Technology*, **9**, 194-202. https://www.scirp.org/pdf/wjet_2021022516304486.pdf https://doi.org/10.4236/wjet.2021.91014

[3] Wang, Y., Voisin, T., McKeown, J., *et al*. (2018) Additively Manufactured Hierarchical Stainless Steels with High Strength and Ductility. *Nature Materials*, **17**, 63-71. https://doi.org/10.1038/nmat5021

[4] Al Mangour, B.A. (2017) Additive Manufacturing of High-Performance 316L Stainless Steel Nanocomposites via Selective Laser Melting. UCLA Electronic Theses and Dissertations. https://escholarship.org/uc/item/4jp76591

[5] Kou, S. (2003) Welding Metallurgy. John Wiley & Sons, Hoboken.

[6] Lancaster, J.F. (1980) Metallurgy of Welding. Allen & Unwin, London. https://doi.org/10.1007/978-94-010-9506-8

[7] Dewidar, M.M., Dalgarno, K.W. and Wright, C.S. (2003) Processing Conditions and Mechanical Properties of High-Speed Steel Parts Fabricated Using Direct Selective Laser Sintering. *Proceedings of the Institution of Mechanical Engineers Part B Journal of Engineering Manufacture*, **217**, 1651-1663.

https://doi.org/10.1243/095440503772680587

[8] Penn, R. (2017) 3D Printing of 316L Stainless Steel and Its Effects on Microstructure and Mechanical Properties. *Graduate Theses & Non-Theses*, 140. http://digitalcommons.mtech.edu/grad_rsch/140

[9] Childs, T., Hauser, C. and Badrossamay, M. (2005) Selective Laser Sintering (Melting) of Stainless and Tool Steel Powders: Experiments and Modelling. *Proceedings of the Institution of Mechanical Engineers*, *Part B*, *Journal of Engineering Manufacture*, **219**, 339-357. https://doi.org/10.1243/095440505X8109

[10] Bunnell, D.E., Das, S., Bourell, D.L., Beaman, J.B. and Marcus, H.L. (1995) Proceedings of the Solid Freeform Fabrication Symposium on Fundamentals of Liquid Phase Sintering during Selective Laser Sintering. The University of Texas, Austin, 440-447.

[11] Guo, N.N. and Leu, M.C. (2013) Additive Manufacturing: Technology, Applications and Research Needs. *Frontiers of Mechanical Engineering*, **8**, 215-243. https://doi.org/10.1007/s11465-013-0248-8

[12] Olakanmi, E.O., *et al*. (2015) A Review on Selective Laser Sintering/Melting (SLS/SLM) of Aluminum Alloy Powders: Processing, Microstructure and Properties. *Progress in Materials Science*, **74**, 401-477. https://doi.org/10.1016/j.pmatsci.2015.03.002

[13] Carlton, H.D., *et al*. (2016) Damage Evolution and Failure Mechanisms in Additively Manufactured Stainless Steel. *Materials Science and Engineering*: *A*, **651**, 406-414. https://doi.org/10.1016/j.msea.2015.10.073

[14] Khairallah, S.A., *et al*. (2016) Laser Powder-Bed Fusion Additive Manufacturing: Physics of Complex Melt Flow and Formation Mechanisms of Pores, Spatter and Denudation Zones. *Acta Materialia*, **108**, 36-45. https://doi.org/10.1016/j.actamat.2016.02.014

[15] Sun, Z.J., *et al*. (2016) Selective Laser Melting of Stainless Steel 316L with Low Porosity and High Build Rates. *Materials & Design*, **104**, 197-204. https://doi.org/10.1016/j.matdes.2016.05.035

[16] Wang, Z.Q., *et al*. (2016) Effect of Processing Parameters on Microstructure and Tensile Properties of Austenitic Stainless Steel 304L Made by Directed Energy Deposition Additive Manufacturing. *Acta Materialia*, **110**, 226-235. https://doi.org/10.1016/j.actamat.2016.03.019

[17] Mirzababaei, S. and Pasebani, S. (2019) A Review on Binder Jet Additive Manufacturing of 316L Stainless Steel. *Journal of Manufacturing and Material Processing*, **3**, 82. https://doi.org/10.3390/jmmp3030082

[18] Kumara, C., Deng, D.Y., Moverare, J. and Nylén, P. (2018) Modelling of Anisotropic Elastic Properties in Alloy 718 Built by Electron Beam Melting. *Materials Science and Technology*, **34**, 529-537. https://doi.org/10.1080/02670836.2018.1426258

[19] Hill, R. (1952) The Elastic Behavior of a Crystalline Aggregate. *Proceedings of the Physical Society. Section A*, **65**, 349-354. https://doi.org/10.1088/0370-1298/65/5/307

[20] Acharya, N., Fatima, B., Chouhan, S.S. and Sanyal, S.P. (2013) First Principles Study on Structural, Electronic, Elastic and Thermal Properties of Equiatomic MTi (M = Fe, Co, Ni). *Chemistry and Materials Research*, **3**, 22-30.

[21] Luan, X.H., Qin, H.B., Liu, F.M., Dai, Z.B., Yi, Y.Y. and Li, Q. (2018) The Mechanical Properties and Elastic Anisotropies of Cubic Ni_3Al from First Principles Calculations. *Crystals*, **8**, 307. https://doi.org/10.3390/cryst8080307

[22] Hertzberg, R.W. (1996) Deformation and Fracture Mechanics of Engineering Materials. 4th Edition, John Wiley, Hoboken.

[23] Broek, D. (1988) Practical Use of Fracture Mechanics. Kluwer, London, 431, 436. https://doi.org/10.1007/978-94-009-2558-8

[24] Lin, W.S. (1974) The Ductile-Brittle Fracture Transformation: A Comparison of Macro and Microscopic Observation on Compact Tension Specimens. Master's Thesis, University of Tennessee, Tennessee.

[25] Gorodtsov, V.A. and Lisovenko, D.S. (2019) Extreme Values of Young's Modulus and Poisson's Ratio of Hexagonal Crystals. *Mechanics of Materials*, **134**, 1-8. https://doi.org/10.1016/j.mechmat.2019.03.017

[26] Svetlov, I.L., Petrushin, N.V., Shchegolev, D.V. and Khvatskiy, K.K. (2010) Anisotropy of Mechanical Properties of Single Crystal in Fourth Generation Ni Base Superalloy. 9*th Liege Conference: Materials for Advanced Power Engineering*, Liège, 27-29 September 2010, 660-667.

[27] Zhang, W.W., Yu, H. and Huang, Q.-A. (2011) Modeling of the Elastic Modulus of Crystalline Silicon Based on a Lattice Dynamics Approach. 2011 16*th International Solid-State Sensors*, *Actuators and Microsystems Conference*, Beijing, 5-9 June 2011, 1416-1419. https://doi.org/10.1109/TRANSDUCERS.2011.5969583

[28] Kamaya, M. (2009) A Procedure for Estimating Young's Modulus of Textured Polycrystalline Materials. *International Journal of Solids and Structures*, **46**, 2642-2649. https://doi.org/10.1016/j.ijsolstr.2009.02.013

[29] Dantzig, J.A. and Rappaz, M. (2016) Solidification (Engineering Sciences, Materials). 2nd Edition, EPFL Press, Lausanne, 319. http://solidification.mechanical.illinois.edu/Figures/macrosegregation.html